Published in final edited form as:

Curr Biol. 2017 July 10; 27(13): 2014–2022.e6. doi:10.1016/j.cub.2017.05.066.

MULTIPLE ISOFORMS OF NESPRIN1 ARE INTEGRAL COMPONENTS OF CILIARY ROOTLETS

Chloe Potter[1], **Wanqiu Zhu**[1], **David Razafsky**[1], **Philip Ruzycki**[1], **Alexander V. Kolesnikov**[1], **Teresa Doggett**[1], **Vladimir J. Kefalov**[1], **Ewelina Betleja**[2], **Moe R. Mahjoub**[2], and **Didier Hodzic**[1,*]

[1]Department of Ophthalmology and Visual Sciences, Washington University School of Medicine, 660 S. Euclid Ave, St Louis, MO 63110, USA

[2]Division of Nephrology, Department of Medicine, Washington University School of Medicine, 660 S. Euclid Ave, St Louis, MO 63110, USA

SUMMARY

SYNE1 (Synaptic nuclear envelope 1) encodes multiple isoforms of Nesprin1 (Nuclear Envelope Spectrin 1) that associate with the nuclear envelope (NE) through a C-terminal KASH (Klarsicht/Anc1/Syne homology) domain (Figure 1A) [1–4]. This domain interacts directly with the SUN (Sad1/Unc84) domain of Sun proteins [5–7], a family of transmembrane proteins of the inner nuclear membrane (INM) [8, 9], to form the so-called LINC complexes (Linkers of the Nucleoskeleton and the Cytoskeleton) that span the whole NE and mediate nuclear positioning [10–12]. In a stark departure from this classical depiction of Nesprin1 in the context of the NE, we report that rootletin recruits Nesprin1α at the ciliary rootlets of photoreceptors and identified asymmetric NE aggregates of Nesprin1α and Sun2 that dock filaments of rootletin at the nuclear surface. In NIH3t3 cells, we show that recombinant rootletin filaments also dock to the NE through the specific recruitment of a ~600 kDa endogenous isoform of Nesprin1 ($Nes1^{600kDa}$) and of Sun2. In agreement with the association of Nesprin1α with photoreceptor ciliary rootlets and the functional interaction between rootletin and Nesprin1 in fibroblasts, we demonstrate that multiple isoforms of Nesprin1 are integral components of ciliary rootlets of multiciliated ependymal and tracheal cells. Together, these data provide a novel functional paradigm for Nesprin1 at ciliary rootlets and suggest that the wide spectrum of human pathologies linked to truncating mutations of *SYNE1* [13–15] may in part originate from ciliary defects.

[*]**CORRESPONDING AUTHOR/LEAD CONTACT** Didier Hodzic, Ph.D., Washington University School of Medicine, Department of Ophthalmology and Visual Sciences, 660 S. Euclid Ave., St. Louis, MO 63110, dhodzic@wustl.edu, Phone: 314-362-7037.

AUTHOR CONTRIBUTIONS

Conceptualization, D.H.; Methodology: D.H., V.J.K., M.R.M.; Investigation: C.P., W.Z, D.R., P.R., A.V.K., T.D., E.B., D.H.; Resources: D.H., V.J.K., M.R.M.; Writing-original draft: D.H.; Writing-review & editing; V.J.K., M.R.M.; Visualization: D.H.; Supervision: D.H., V.J.K., M.R.M; Project administration: D.H.; Funding acquisition: D.H.

Keywords

SYNE1; Nesprin1; Nesprin2; Sun1; Sun2; LINC complexes; nuclear envelope; rootletin; rootlets; basal bodies; cilia; photoreceptors; retina

RESULTS AND DISCUSSION

Nesprin1 forms filamentous structures in photoreceptors

We recently established that a variant of Nesprin1 giant devoid of KASH domain localizes at large cerebellar synapses between afferent mossy fibers and cerebellar granule neurons [16]. The noncanonical localization of this protein beyond the NE led us to further examine the origin of filamentous structures we routinely observed both in the inner segment (IS) and the outer nuclear layer (ONL) of photoreceptors (Figure 1B, upper left panel and Figure S1A and S1B) with a Nesprin1 antibody whose epitope overlaps with the C-terminal region of Nesprin1 giant, α and β isoforms (Nes1HAA12, Figure 1A). The Nesprin1 immunoreactivity in the IS was rather striking as this compartment is devoid of nuclei. However, proteomic studies of the photoreceptor sensory cilium, which extends throughout the IS and outer segment (OS), reported numerous tryptic peptides encoded by the C-terminal region of *Syne1* [17]. The Nesprin1 immunoreactivity in the ONL, which consisted of smaller curved filaments (Figure 1B and S1A) also suggested that Nesprin1 localized asymmetrically at the NE of photoreceptors.

To exclude ant nonspecific cross-reactivity of our Nesprin1 antibody with these structures, *Syne1* was inactivated in rods by crossing a strain harboring LoxP sites flanking exon-16 of *Syne1* (*Nes1*$^{F/F}$, Figure 1A) with a Rho-*Cre* strain that initiates rod-specific Cre recombinase expression under the control of a rhodopsin promoter at postnatal day 6 (P6) [18, 19]. As shown in Figure 1B and S1A, the Nesprin1 immunoreactivity was absent both from the IS and the ONL of $^{Rho\text{-}Cre}Nes1^{\Delta/\Delta}$ rods thereby confirming that these filamentous structures were encoded by *Syne1*. The Nesprin1 immunoreactivity in cones of $^{Rho\text{-}Cre}Nes1^{\Delta/\Delta}$ retinas further emphasized similar filamentous structures lining the IS as well as complex “aster-like” structures capping the apical side of cone nuclei (Figure 1B, lower panels and Figure S1A). These structures were undetectable in $^{Actin\text{-}Cre}Nes1^{\Delta/\Delta}$ retinas where *Syne1* is inactivated both in rods and cones (Figure 2D, inset 3′). However, a strong staining of cones outer segments (OS), whose origin remains uncertain, persisted in these conditions (Figure S1A). These data emphasized a noncanonical localization of Nesprin1 in photoreceptors.

Nesprin1α is the main components of rods filamentous structures

Nesprin1α (~120 kDa), Nesprin1β (~350 kDa) and Nesprin1 giant correspond to multiple isoforms encoded by *SYNE1* through the use of distinct internal promoters [3, 20–22]. As shown in Figure 1C, an immunoreactive band of ~120 kDa was depleted from $^{Rho\text{-}Cre}Nes1^{\Delta/\Delta}$ retinal lysates. This 120 kDa protein was also depleted from retinal lysates of rhodopsin KO retinas that lack cone and rod photoreceptors (Figure S1C). It also co-segregated with IS/OS purified from whole retinas (Figure S1D). These approaches suggested that this ~120 KDa protein accounted for the non-canonical immunoreactivity of

Nesprin1 in photoreceptors. Further findings supported that this protein corresponds to Nesprin1α. First, a promoter located just upstream the first exon of Nesprin1α becomes activated and Nesprin1α transcripts upregulated upon photoreceptor differentiation at late stages of retinal development (Figure 1D), and we previously identified this 120 kDa protein as Nesprin1α by mass spectrometry [23]. In addition, photoreceptors did not display any immunoreactivity with a Nesprin1 antibody whose epitope overlaps with larger isoforms of Nesprin1 (Nes1QFA13, Figure 1A and data not shown). Finally, we directly confirmed the synthesis of Nesprin1α transcripts in the retina by RT-PCR (Figure 1E). In agreement with previous studies [21, 24], the expression pattern of Nesprin1α transcripts was mostly restricted to cardiac and skeletal muscle although low levels of Nesprin1α transcripts were also detected in the cerebellum (Figure S1E, F). The noncanonical localization of Nesprin1α in photoreceptors IS suggested that at least a fraction of Nesprin1α transcripts would display the alternative splicing of exon-2, which is indicative of Nesprin1 isoforms devoid of KASH domain [16, 23]. However, XbaI digests of Nesprin1α transcripts (Figure 1E), used to monitor the status of exon-2 (Figure S1E), and direct sequencing of retinal Nesprin1α amplicons failed to reveal any alternative splicing of exon -2 in Nesprin1α transcripts amplified from retina, skeletal and cardiac muscles (Figure S1F).

Depletion of Nesprin1α affects rod photoreceptor function

To evaluate the functional consequences of Nesprin1α depletion in rods, electroretinograms were acquired from 2.5 months-old $^{Rho\text{-}Cre}Nes1^{\Delta/\Delta}$ and $^{Rho\text{-}Cre}Nes1^{\Delta/WT}$ littermates. As shown in Figure 1F, the amplitudes of scotopic a-waves (a measure of the light-dependent hyperpolarization of rods) and b-waves (a measure of rod bipolar cell depolarization ensuing rod hyperpolarization) were modestly but significantly decreased in $^{Rho\text{-}Cre}Nes1^{\Delta/\Delta}$ by comparison to $^{Rho\text{-}Cre}Nes1^{\Delta/WT}$ suggesting that Nesprin1α-based filamentous structures are relevant to photoreceptors function. Of note, the lack of Nesprin1 expression did not obviously affect the thickness of the outer nuclear layer, an indicator of rod degeneration, or the overall morphology of 2.5 month-old $^{Rho\text{-}Cre}Nes1^{\Delta/\Delta}$ rods (Figure S1A and data not shown).

Nesprin1α recruits rootletin filaments at the nuclear periphery of rod photoreceptors

The localization pattern of Nesprin1α in photoreceptors IS and ONL was reminiscent of the distribution of rootletin [25], the main component of ciliary rootlets that form exceptionally long striated filaments and span the whole IS of photoreceptors (Figure 2A). Immunogold labeling showed that Nesprin1α colocalized with striated filaments of rootletin (Figure 2B). Within the ONL, we further observed finite electron-dense striated filaments that lined the periphery of rod nuclei (Figure 2C). Accordingly, the filamentous patterns of Nesprin1α and rootletin extensively overlapped both within IS (Figure 2D, compare insets 1′ and 1″) and the ONL (Figure 2D, compare insets 2′ and 2″). Interestingly, in $^{Actin\text{-}Cre}Nes1^{\Delta/\Delta}$ retinas, which lack Nesprin1α in the IS (Figure 2D, compare insets 1′ and 3′) and the ONL (Figure 2D, compare insets 2′ and 4′) of both rods and cones, rootletin filaments were undetectable in the ONL (compare insets 2″ and 4″). By contrast, the lack of Nesprin1α did not seem to affect the localization of rootletin in the IS (Figure 2D, compare insets 1″ and 3″). These data indicated that Nesprin1α colocalized with photoreceptors ciliary rootlets that line the IS and with finite rootletin filaments that appeared intimately associated with the NE of rods.

We further confirmed that the loss of perinuclear rootletin filaments in $^{Actin\text{-}Cre}Nes1^{\Delta/\Delta}$ photoreceptors originated from the docking of rootletin filaments by Nesprin1α at the nuclear surface. We first asked whether Nesprin1α actually associated with the NE of rods in a KASH-dependent manner using a mouse strain that conditionally expresses a recombinant KASH domain fused to EGFP (hereafter called EGFP-KASH, [26]). EGFP-KASH acts in a dominant-negative manner on endogenous SUN/KASH interactions and, as a result, displaces endogenous Nesprins from the NE [27, 28]. Expression of EGFP-KASH was induced with the Chx10-*Cre/GFP* strain that expresses a Cre-recombinase (fused to EGFP) transiently in most embryonic retinal progenitors and permanently in adult bipolar cells [29]. As expected, Nesprin1α was detected both in the IS and the ONL of control Chx10-Cre/EGFP retinas (Figure 2E, top panel). By contrast, rod nuclei expressing EGFP-KASH were devoid of Nesprin1α (Figure 2E, bottom panels) whereas Nesprin1α was still detected at nuclei of non-recombinant rods of $^{Chx10\text{-}Cre}$EGFP-KASH retinas (Figure 2E, arrows). Of note, the localization of Nesprin1α in the IS appeared unaffected by the expression of EGFP-KASH. In agreement with the loss of perinuclear rootletin staining in $^{Actin\text{-}Cre}Nes1^{\Delta/\Delta}$, perinuclear rootletin filaments were absent from EGFP-KASH-positive rod nuclei but still present at the nuclear periphery of EGFP-KASH-negative rods (Figure 2F). Together, these findings indicated that asymmetric aggregates of Nesprin1α associate in a KASH-dependent manner with the NE of rods where they dock perinuclear rootletin filaments. Even though we can't formally exclude that Nesprin1α may be required for the polymerization of perinuclear rootletin filaments, the loss of Nesprin1α did not seem to affect the immunofluorescence pattern of rootletin in photoreceptors IS (Figure 2D, inset 3″).

Recombinant rootletin filaments aggregate SUN2/Nesprin1 LINC complexes

We investigated how Nesprin1α could possibly aggregate asymmetrically at the NE or form long filamentous structures beyond the NE of rods since the canonical localization of Nesprin1 isoforms consists of a homogenous distribution at the NE (Figure S2C). As Nesprin1α invariably colocalized with rootletin filaments of photoreceptors, we hypothesized that rootletin filaments mediated this unusual localization of Nesprin1α. Since striated rootletin filaments assemble in cells transfected with a Myc-tagged version of rootletin (Myc-Root) [30], the latter was transfected into NIH3t3 fibroblasts that express a ~600kDa endogenous isoform of Nesprin1 ($Nes1^{600kDa}$) at their NE (Figure S2C). Myc-Root preferentially associated with the centrosome (asterisk, Figure 3A) where it formed complex structures with $Nes1^{600kDa}$ (Figure S2A, B). In addition, Myc-Root also formed branched and unbranched filaments that overlapped with the nucleus. Interestingly, these filaments induced a dramatic redistribution of $Nes1^{600kDa}$ into aggregates that colocalized with Myc-Root filaments both on the apical and basal side of the NE (Figure 3A and S2D). We did not observe any redistribution of either Nesprin2 (Figure 3B and S2E), a structural homolog of Nesprin1, or of Sun1 (Figure 3C and S2F) in the same conditions. By contrast, Sun2 was recruited into $Nes1^{600kDa}$/Myc-root filaments (Figure 3D and S2G) suggesting that Myc-Root filaments induce the aggregation and interact with Sun2/$Nes1^{600kDa}$ LINC complexes at the NE. In agreement with this model (Figure 3E), we detected discrete arrays of Sun2 aggregates that colocalized with Nesprin1α at the NE of rods (Figure 3F). In addition, Myc-Root was unable to associate with the NE of NIH3t3 depleted of $Nes1^{600kDa}$

(Figure 3G) even though Myc-Root still formed filaments in the cytoplasm. Finally, and similarly to what we observed in rods, expression of dominant-negative EGFP-KASH2 in NIH3t3 cells also prevented the docking of rootletin filaments at the NE (Figure S2H). Thus, similarly to the requirement of Nesprin1α to dock perinuclear rootletin filaments in rod photoreceptors, Nes1^{600kDa} appears to provide a unique docking site for Myc-Root filaments at the NE of NIH3t3 cells. Of note is that the expression of Nes1^{600kDa} was also required (data not shown) for the indiscriminate relocalization of Nesprin2, Sun1 and Sun2 at the centrosome of Myc-Root transfected cells (arrows in merged panels of Figure 3A–D and data not shown).

To gain more insight into the interaction mechanisms between Nesprin1α, which is not expressed in NIH3t3 fibroblasts (Figure S1F and S2C), and rootletin, EGFP-Nesprin1α and Myc-Root were coexpressed in NIH3t3 cells. As shown in Figure 3H, EGFP-Nesprin1α and Myc-Root filaments colocalized and formed a complex meshwork that surrounded the nucleus. The KASH domain was not required for this colocalization as EGFP-Nesprin1αΔKASH, which lacks the KASH domain, extensively colocalized with Myc-Root filaments in the cytoplasm of NIH3t3 cells (Figure 3I). These data suggested that the cytoplasmic region of Nesprin1α is sufficient to interact with rootletin. We examined this interaction further. Even though Myc-Root was insoluble in RIPA buffer, deletion mutants of Myc-Root proved partially soluble (Figure 3J) and allowed for immunoprecipitation assays. As shown in Figure 3K, Myc-Root C-1-3 and Myc-Root C1-2 coimmunoprecipitated with EGFP-Nesprin1αΔKASH as well as with endogenous Nes1^{600kDa} (Figure S2I). These results suggest that the aggregation of multiple isoforms of Nesprin1 by rootletin occurs through the interaction between the N-terminal region of rootletin encompassing coiled-coil domains 1 to 3 (Figure 3J) and the cytoplasmic region encoded by exon-16 to exon-2 of *Syne1* (Figure S1E).

Multiple isoforms of Nesprin1 associate with ciliary rootlets of multiciliated cells

Next, we examined whether Nesprin1 localized at the ciliary rootlets of other ciliated cell types. As shown in Figure 4A, Nesprin1 formed linear arrays on the apical surface of multiciliated ependymal cells that line the lumen of brain ventricles. This localization was clearly distinct from the NE labeled with lamin B1 (Figure 4A, yellow arrows in inset). Furthermore, this Nesprin1 immunoreactivity colocalized with ciliary rootlets labelled with rootletin (Figure 4B) and just below ciliary axonemes labeled with acetylated tubulin (Figure 4C). This signal was specific as Nesprin1 immunoreactivity was absent at ciliary rootlets of ependymal cells in $^{Actin\text{-}Cre}Nes1^{\Delta/\Delta}$ brains (Figure 4D). Interestingly, Nesprin1α transcripts are not expressed in the cerebrum whereas transcripts from both KASH and KASH-LESS variants of larger Nesprin1 isoforms are readily detected by RT-PCR (Figure S1F). In agreement with these data, ependymal cells display strong *in situ* hybridization with *Syne1* probes that recognize large isoforms of Nesprin1 (experiment 74640879, Allen Mouse Brain Atlas [31]). These data suggest that large Nesprin1 isoforms are integral components of ciliary rootlets of ependymal cells. Finally, multiciliated tracheal epithelial cells (MTEC) differentiated *in vitro* [32] also displayed a strong Nesprin1 immunoreactivity that colocalized with rootletin just underneath basal bodies labeled with centrin (Figure 4E).

Together, these results indicated that multiple isoforms of Nesprin1 are conserved components of ciliary rootlets.

In summary, we uncovered a novel functional interaction between multiple isoforms of Nesprin1 and rootletin. In light of the role of rootlets in the maintenance of ciliary functions [33–35], this new biological paradigm for Nesprin1 at ciliary rootlets is of significant clinical significance. Indeed, biallelic truncations of *SYNE1* underlie autosomal recessive cerebellar ataxia Type I (ARCA1), a progressive form of pure cerebellar ataxia that consists of limb and gait ataxia, dysarthria and severe cerebellar atrophy [13, 36, 37]. More recent studies have emphasized that these cerebellar pathologies are most often accompanied by variable combinations of multisystemic pathologies that include upper and lower motor neuron disease, muscle atrophy and spasticity, kyphoscoliosis, respiratory distress and neurocognitive disorders [14, 15, 38–40]. The molecular pathogenesis of these mutations is currently unknown but our results suggest that at least a subset of these pathologies may be linked to a loss of function of ciliary Nesprin1. To that respect, several pathologies associated with *SYNE1* mutations include respiratory distress, kyphoscoliosis or mental retardation [14, 15], a set of phenotypes commonly associated with human ciliopathies [41]. The docking of rootletin filaments by SUN2/Nesprin1 LINC complexes has many biological implications. First, it represents a novel NE “coupling device” similar to transmembrane-associated nuclear (TAN) lines that couple the nucleus to cytoplasmic actin fibers via Sun2/Nesprin2 giant LINC complexes [42, 43]. How Sun2, but apparently not Sun1, is selectively incorporated into rootletin-based LINC complexes or in TAN lines is striking as there is no evidence to date of a selective pairing between the SUN and KASH domains of specific Nesprins and Sun proteins [27]. Second, the association of rootletin with the NE suggests additional *in vivo* functions for rootletin beyond ciliary rootlets. To that respect, Espigat-Georger and colleagues recently reported that Nesprin1 is essential for the NE relocalization of centrosomal proteins such as PCM-1 during myoblasts differentiation [44]. Finally, our RT-PCR experiments in photoreceptors indicating that rootlet-associated Nesprin1α may harbor a KASH domain (Figure 1E and S1E, F) and the recruitment of all endogenous LINC complex components at Myc-Root centrosomes (Figure 3 A–D) suggest the provocative hypothesis that SUN/KASH interactions may actually take place beyond the NE in specific physiological settings. Future studies will help to determine the prevalence and functional relevance of these novel rootletin-based LINC complexes *in vivo*.

STAR METHODS

CONTACT FOR REAGENT AND RESOURCE SHARING

Further information and requests for resources and reagents should be directed to and will be fulfilled by the Lead Contact, Didier Hodzic (Dhodzic@wustl.edu) via applicable Washington University Material Transfer Agreements and/or licensing agreements through the Office of Technology Management at Washington University School of Medicine.

EXPERIMENTAL MODEL AND SUBJECT DETAILS

Animals—Rho-*Cre*, *Rho*$^{-/-}$, Chx10-*Cre* (Line 2) and Actin-Cre transgenic mice were obtained directly or indirectly from Drs. C.K. Chen, R.L. Sidman, C. Cepko and G.R.

Martin [18, 29, 45, 46], respectively. Nesprin1$^{F/F}$ mice were a kind gift of Dr. J. Chen [19]. EGFP-KASH2 mice (Tg (CAG-LacZ/EGFP-KASH2)) were developed in our laboratory [26, 47]. For each experimental model tested, multiple littermates (1 to 3 month-old) were selected based on appropriate genotype (test or control group). All experiments were repeated on littermates of at least two distinct litters. The same experimental outcome was observed irrespective of gender. A $^{Rho\text{-}Cre}$Nes1$^{\Delta/\Delta}$ test group of 2 males and 2 females and a $^{Rho\text{-}Cre}$Nes1$^{\Delta/wt}$ control group of 1 male and 3 females were used to acquire electroretinograms. All mice were housed at the Mouse Genetic Core barrier facility (Dr. M.Wallace) located at the East McDonnell Building. None of the mice used in our experiments were involved in previous procedures. The health status of our mouse colony is monitored weekly by a veterinarian from the Division of Comparative Medicine that also supervises mice procurement, quarantine, acclimation and husbandry. Washington University is accredited by the American Association of Laboratory Animal Care (AALAC) with several trained veterinarians and an extensive support staff. Animal protocols used in this project strictly adhere to the ethical and sensitive care and use of animals in research and were approved by the Washington University School of Medicine Animal Studies Committee (Animal Welfare Assurance Permit # A-3381-01, Protocol# 20160171).

Cell Lines—NIH3t3 fibroblasts (ATCC#CRL-16580, male) were purchased from the American Type Tissue Collection through the Tissue Culture Support Center at Washington University School of Medicine. They were cultured in DMEM (Sigma-Aldrich) supplemented with 10% fetal bovine serum (Atlanta Biologicals), 100U/ml of penicillin and 100μg/ml of streptomycin (Thermofisher).

METHODS DETAILS

Generation of antibodies against Nesprins and Sun proteins—Myc (clone 9E10, #SC-40), lamin B1 (C20, #SC-6216), Gαt1 (K-20, #SC-389) and rootletin (C20, #SC-67824) antibodies were purchased from Santa Cruz Biotechnology, RDH10 (#14644) from Proteintech, CAR (#AB15282) and centrin (#04-1624) from Millipore and γ-tubulin (clone GTU-88, #T6557) and acetylated tubulin (clone 6-11B-1, #T7451) from Sigma-Aldrich. Mouse (Nes1M5) and rabbit (Nes1Rb4) anti-Nesprin1 antibodies were raised against an epitope of 882 amino acids located upstream the KASH domain of mouse Nesprin1α, rabbit anti-Nesprin2 antibodies were generated against an epitope of 468 amino acids located upstream the KASH domain of mouse Nesprin2 and rabbit Sun1 antibodies were generated against an epitope of 211 amino acids overlapping with the coiled-coil domain of the luminal region of mouse Sun1. As previously described [23, 48, 49], the cDNAS corresponding to these epitopes were amplified by RT-PCR from total RNA extracted from C2C12 cells, cloned in frame with an N-terminal GST fusion protein in PGEX-4T-1 (GE Healthcare) and sequenced. IPTG induction of GST fusion proteins synthesis was performed in competent BL21 E. Coli. Fusion proteins were extracted from inclusion bodies in urea, separated on a Superdex200 column (GE Healthcare, Pittsburgh, PA, USA) and concentrated using an Amicon Ultracell 10k (Sigma-Aldrich). Purified GST fusion proteins were used for immunization at PRIMM Biotech (Cambridge, MA, USA). The rabbit polyclonal antibody against mouse Sun2 was generated against a Histidine tagged epitope of 230 amino acids overlapping with the luminal coiled-coil domains (encoded by

exon 7 to 12) of mouse Sun2. The recombinant epitope was synthesized and used for immunization at PRIMM Biotech. Nesprin1, Nesprin2, Sun1 and Sun2 antibodies described above were rigorously validated as shown in Figure S2C for Nesprin1 antibodies.

Immunofluorescence microscopy of retinal slices—Retinas were isolated from mice processed for transcardial perfusion with 4% PFA as previously described in details [50]. Briefly, after anesthesia, an incision was performed from the lower abdomen to the top of the rib cage to gain access to the heart. After performing a small incision in the right atrium of the heart, a 30% sucrose/PBS solution was perfused into the left ventricle at a rate of ~2–5 ml per min. The same perfusion was then performed with a 4% parafolmadehyde/PBS solution and the retinas dissected out. For antibodies that required methanol fixation (rootletin and γ-tubulin), mice were euthanized by CO2 inhalation and dissected retinas incubated in methanol at −20°C for 30 min. After fixation, PFA- or methanol-fixed retinas were processed for immunofluorescence as previously described in details [50]. Briefly, 15 μm Optimal Cutting Temperature (OCT) sections were rinsed three times in PBS, permeabilized in blocking buffer (10% donkey serum/0.5% Triton X-100 in PBS) for 30 min and incubated overnight with primary antibodies diluted in blocking buffer. After several washes with PBS, sections were incubated with highly cross-adsorbed Alexa 488, 594 and 647 secondary antibodies raised in donkey (Thermofisher) for 1 h in blocking buffer. After several washes in PBS and DAPI staining, slices were mounted in anti-fading mounting medium (DAKO). To separate the IS/OS interface from the retina, dissected retinas were vortexed in PBS/30% sucrose. IS/OS were separated from the retinal bulk by collecting the post-centrifugation (3,000g for 5 min) supernatant. Volume/volume aliquots of pelted retina and IS/OS supernatants were analyzed by SDS-PAGE.

Cell culture, transfections and immunofluorescence microscopy—Transfections were performed on ~70% confluent NIH3t3 cells plated on glass coverslips in 24-well plates. For each well, 500 ng of plasmid in 25 μl OPTIMEM (Thermofisher) was added to another aliquot of 25 μl OPTIMEM supplemented with 1.5 μl Lipofectamine 2000 (Thermofisher). The mixture was incubated for 5 minutes at room temperature and added dropwise to each well. Cells were incubated for 16 h before immunofluorescence analysis. Nesprin1 downregulation in NIH3t3 was performed with a Dicer-substrate short interfering RNAs (DsiRNAs, 27 mer duplexes, TrifectA RNAi kit mm.Ri. Syne1.13, Integrated DNA Technologies) whose target sequence is located within exon -13 (Figure S1E) of NM_022027. A DsiRNA against hypoxanthine-guanine phosphoribosyltransferase (HPRT) was used as a control. DsiRNA transfections (20 nM final concentration) of NIH3t3 cells were performed with Lipofectamine SiRNAMax (Thermofisher) for 48h before immunoblot and immunofluorescence analysis. Myc-root transfection of DsiRNA-transfected cells was performed 32 h after the initial DSiRNA transfection before returning cells to the incubator for another 16 h. For immunofluorescence microscopy, coverslips were rinsed three times with PBS and fixed for 10 min either at room temperature in 4% paraformaldehyde (Electron Microscopy Sciences) or at −20 C in a 1:1 methanol: acetone solution. Cells were then rinsed and processed with primary and secondary Alexa antibodies. All experiments performed with NIH3t3 cells were repeated at least three times with the same experimental outcome. Multiciliated mouse tracheal epithelial cells (MTECs) were isolated, cultured and

differentiated as previously described in details [32, 51]. Briefly, trachea were excised from adult C57BL/6J mice, opened longitudinally to expose the lumen, and placed in 1.5 mg/ml pronase E (Sigma-Aldrich) in F12K nutrient mixture (ThermoFisher) at 4°C overnight. Tracheal basal cells were dislodged by gentle agitation and collected in F12K with 10% FBS. After centrifugation, cells were treated with 0.5 mg/ml DNase I (Sigma-Aldrich) for 5 min on ice and centrifuged at 4°C for 10 min at 400 *g*. Cells were resuspended in DMEM/F12 (ThermoFisher) with 10% FBS and plated in a tissue culture dish for 3 h at 37°C with 5% CO_2 to adhere contaminating fibroblasts. Nonadherent cells were collected, concentrated by centrifugation and resuspended in MTEC-complete medium composed of the following: DMEM/F12 supplemented with 5% FBS, 1.5 mM L-Glutamine (ThermoFisher), 0.3% sodium bicarbonate (ThermoFisher), 10 μg/ml Insulin (Sigma-Aldrich), 25 ng/ml Epidermal growth factor (BD Biosciences), 5 μg/ml apo- Transferrin (Sigma-Aldrich), 0.1 μg/ml Cholera toxin (Sigma-Aldrich), 30 μg/ml bovine pituitary extract (Hammond Cell Tech), and 50 nM retinoid acid (Sigma-Aldrich). Cells were seeded onto Transwell-Clear permeable filter supports (Corning). Air-liquid interface (ALI) was established 2 d after cells reached confluence by feeding MTEC serum-free medium only in the lower chamber. Cells were cultured at 37°C with 5% CO_2, and the media replaced every 2 days. All media were supplemented with 100 U/ml penicillin-100 mg/ml streptomycin (ThermoFisher), and 0.25 mg/ml Fungizone (ThermoFisher).

Recombinant constructs—The Myc-root plasmid (pRcCMV Rootletin [30]) was a kind gift from Dr. E. Nigg (Addgene#41167). Root C1-4 and Root C1-3 inserts respectively correspond to FseI/SmaI and FseI/BbsI restriction fragments isolated from the original pRcCMV-Rootletin vector. Root C1-2 was amplified by PCR from the pRcCMV-Rootletin vector with FseI- and NotI-flanked primers. All inserts were cloned back into the FseI and NotI restriction sites of the original vector. cDNAs of Nesprin1α and of Nesprin1αΔKASH (lacking exon-2) were amplified by RT-PCR from mouse cerebellum and both cloned in the pEGFP-C3 vectors (Clontech). EGFP-KASH2 and EGFP-KASH2ext constructs have been described previously [27].

Electron microscopy—To visualize the rootletin network in photoreceptors IS, dissected retinal cups were incubated for 24h in cold fixative solution (2.5% glutaraldehyde/0.1M cacodylate/2.5mM CaCl2, pH 7.4). The fixative solution was rinsed out with several exchanges with 0.1 M cacodylate buffer over a 3 hr period and then stained with 1% OsO_4/0.1 M cacodylate for one hour in the dark with rotation. OsO_4 was washed out with 3 rinses with 0.1 M cacodylate (15 minutes each) followed by 3 rinses in H_2O over 30 minutes and then dehydrated with 20%, 40%,60%,80% ethanol solutions, 20 minutes each. Samples were then place in 100% ethanol overnight at 4°C, transferred into fresh 100% ethanol, followed by two exchanges of 100% propylene oxide, 15 minutes each. Samples were infiltrated in Araldite resin (EMS, Hatfield, PA) in increments of 25%, 50%, 75% resin/ propylene oxide for one hour and further incubated overnight in 100% resin at room temperature. Samples were placed into blocks and cured at 60°C overnight. Blocks were sectioned on an ultra-microtome at an 80 nm thickness, post stained with 2% Uranyl Acetate for 2 minutes and Reynolds lead citrate for 2 minutes. Sections were viewed on a JEOL 1400 transmission microscope and imaged with an AMT digital camera. To visualize rods

perinuclear rootletin filaments, retinas were dissected and fixed in 4% PFA/0.5% glutaraldehyde/0.1M Sorensons buffer (pH7.4) for 24h at 4°C and successively incubated in a series of graded sucrose solutions in 0.1M Sorensons buffer (10% for 30 min, 20% for 30 min, 30% for 1h, then fresh 30% overnight at 4°C). Retinas were then freeze/thawed 3 times in 30% sucrose solution using dry ice and a 37°C water bath, cut in half sagitally, washed twice with 0.1M cacodylate buffer (pH7.3), post-fixed with 1% osmium tetroxide, then with 2% uranyl acetate, dehydrated in a graded series of ethanol followed by propylene oxide and embedded in Araldite 502 resin.

Immunogold electron microscopy—Retinas isolated from mice processed for transcardial perfusion with 4% PFA were embedded and cooled down in 4% low melt agarose (Sigma-Aldrich). Agarose blocks (150 μm) were sliced on a vibratome (VT100S, Leica), collected in TBS, permeabilized in blocking buffer (0.5%saponin/10% donkey serum/1X TBS) for 30 min at room temperature and incubated overnight at 4°C with anti-Nesprin1 antibodies in blocking buffer. Slices were then washed three times in 1X TBS and further incubated for 18h with Rabbit Fab coupled to Alexa 594 Fluoronanogold particles (Nanoprobes). After three washes in TBS, retinal slices were transferred to 2% glutaraldehyde, rinsed twice in PBS for 30 min and twice in H2O twice for 5 min, incubated in in 0.02M sodium citrate buffer, pH 4.8 three times for 5 min. Samples were then developed with HQ Silver Enhancement Kit (Nanoprobes) for 9 minutes, followed by rinses two H2O rinses for 5 minutes before post-fixation with 1% OSO4/dH2O for 30 minutes. After three rinses in dH2O, samples were dehydrated with ethanol as described above and infiltrated with increments of 25%, 50%, and 75% LX112 resin in ETOH (1 hr per exchange) with final placement in 100% LX112. Samples were then mounted between two Teflon coated slides in LX112 resin and polymerized over night at 60°C. Samples were removed from slide mounts, glued onto resin stubs, and sectioned at an 80 nm thickness as described above.

Immunoblotting and immunoprecipitations—Dissected retinas were immediately bead-beaten in 200 μl of Laemli buffer/5% β-mercaptoethanol with zirconium beads, centrifuged at maximum speed for 10 min and boiled for 5 min before SDS-PAGE analysis. Transfected NIH3t3 cells were rinsed three times in PBS, resuspended and immediately boiled in laemli buffer/5% β-mercaptoethanol. Protein lysates separated by SDS-PAGE were transferred to Optitran nitrocellulose membranes (GE Healthcare) that were blocked with 5% milk in TBST for 1 hour at room temperature and incubated overnight at 4°C with Nesprin1 antibodies. After three washes with TBST, membranes were incubated with HRP-conjugated secondary antibodies. Signals were detected using SuperSignal® West Pico solutions (Thermofisher) and exposed on X-ray films. Films were digitized using a G: Box HR16 imaging system (Syngene). Vertical Agarose Gel Electrophoresis was performed as previously described [16]. For immunoprecipitation, NIH3t3 cells were transfected for 16 h with Myc-root deletion constructs either alone or with Nesprin1αΔKASH as described above. Cells were lysed in modified RIPA buffer (1% Tritonx-100, 0.1%SDS, 1mM EDTA in PBS) supplemented with protease inhibitors (Complete Mini, Roche). Lysates were centrifuged and the supernatant cleared with 30 μl of A/G beads slurry (Pierce Protein A/G Plus Agarose) for 4 h. Cleared supernatants were then incubated overnight with 15 μl of A/G

beads slurry and 2 μg of either Nesprin1 antibody or rabbit immunoglobulins used as a negative control. Beads were then washed three times 5 min in PBS, boiled and reduced in 1X Laemmli buffer/5% β-mercaptoethanol. Forty percent of each immunoprecipitation was immunoblotted with Myc and/or EGFP monoclonal antibodies. Immunoblotting and immunoprecipitation experiments were repeated at least twice.

RNA extraction and transcripts analyses—Tissues (100 mg of wet weight or 2 retinas) dissected from a 2 month-old C57/Bl6 mouse were resuspended in 1 ml of Trizol (Thermofisher) supplemented with zirconium beads, bead-beaten with a Bullet Blender (Next Advance) and centrifuged. Total RNA was purified from supernatant according to the manufacturer's specifications, reverse transcribed with Superscript II (Thermofisher). Two μl of each RT reaction was amplified with Taq Hi-FI polymerase (Thermofisher). Thirty amplification cycles were performed using either primer p1532 (Nesprin1α 5′-TCCAGGAAGGACTGAGCCTT-3′) or p1350 (Longer Nesprin1 isoforms, 5′-GAGAACAAAATCCAGCTTCAGGAAATGGGAGAACGGC-3′) in combination with primer p1535 (3′UTR, 5′-CTTGTGTGGGGATGTCTGCT-3′). Thirty-five amplification cycles were further repeated on retina RT reactions to compensate for the lower yield of total RNA extracted from retinal tissues. XbaI restriction digests were performed on 10 μl of RT-PCR reactions. These experiments were performed independently on two C57/Bl6 mouse with the same experimental outcome.

Image acquisition—Light microscopy images were acquired (single field and *z*-stacks) with a Nikon Eclipse Ti inverted microscope coupled to an LED light source (Lumencor) and an X-light spinning disk (Crest Optics) with the NIS element software package (Nikon) using 40× (N.A. 1.4) or 100X (N.A. 1.45) objectives. Ependymal cells in Figure 4A were imaged on a Nikon A1Rsi confocal microscope with the 100X (N.A. 1.45) objective.

Electrophysiology—ERGs were acquired from both eyes of 4 mice of the $^{Rho\text{-}Cre}$Nes1$^{\Delta/\Delta}$ test group and of 4 mice of the $^{Rho\text{-}Cre}$Nes1$^{\Delta/wt}$ control group. All mice originated from three distinct litters. Mice were dark-adapted overnight and anesthetized with an intraperitoneal injection of a mixture of ketamine (100 mg/kg) and xylazine (20 mg/kg). Pupils were dilated with a drop of 1% atropine sulfate. Body temperature was maintained at 37°C with a heating pad. ERG responses were measured from both eyes by contact corneal electrodes held in place by a drop of Gonak solution. Full-field ERGs were recorded with the UTAS BigShot apparatus (LKC Technologies) using Ganzfeld-delivered test flashes of calibrated 530 nm LED light (within a range from 2.5×10-5 cd·s m-2 to 23.5 cd·s m-2).

QUANTIFICATION AND STATISTICAL ANALYSES

ERG analyses—The amplitude of the a-wave was measured from the pre-stimulus baseline to the primary peak of negative polarity voltage. The amplitude of b-wave was determined from the a-wave peak to the maximum of the secondary positive peak. Data were expressed as means ± SEMs. Unless stated otherwise, data were analyzed with Origin 8.5 software using the independent two-tailed Student's *t* test, with an accepted significance level of $P < 0.05$.

RNAseq and DNase I hypersensitivity analyses—Raw RNAseq data were obtained from previously published studies [GEO: GSE52006, GSE65506] [52, 53]. Reads were aligned to the mouse genome (version mm9) with TopHat2 (v.2.0.5) [54] using the following parameters: –a 5 -m 1 -i 10 -I 500000 -r 100 – p 4 –microexon-search –no-coverage-search -x 20 –segment-length 25. Dependencies included Bowtie (v.0.12.8) [55] and Samtools (v. 0.1.18) [56]. Bed files were visualized using IGV [57]. Exon coverage was calculated using BEDTools (v.2.23.0) [58] for the region (mm9: chr 10:5,277,478-5,277,734) which was defined by RefSeq annotation and by visual inspection of the mapped reads. For Dnase1 Hypersensitivity, mapped bam files were obtained from ENCODE [GEO: GSM1014198, GSM1014175, GSM1014188] [59]. Coverage was determined using BEDTools (v.2.23.0) [58] for the region centered on the peak of DNase I hypersensitivity overlapping exon -16b (mm9: chr10:5,276,885-5,277,885) and normalized to total mapped reads (reads per million, RPM). Data represents a smoothed view of reads per base per million (window: 50bp).

KEY RESOURCES TABLE

REAGENT or RESOURCE	SOURCE	IDENTIFIER
Antibodies		
Mouse monoclonal anti-Myc	Santa Cruz	9E10; Cat#SC-40
Goat polyclonal anti-lamin B1	Santa Cruz	C20; Cat#SC-6216
Rabbit polyclonal anti-Gαt1	Santa Cruz	K20; Cat#SC-389
Goat polyclonal anti-rootletin	Santa Cruz	C20; Cat#SC-67824
Mouse monoclonal anti-EGFP	Santa Cruz	B2; Cat#SC-9996
Rabbit polyclonal anti-Cone arrestin (CAR)	Millipore	Cat#AB15282
Mouse monoclonal anti-Centrin	Millipore	Clone 20H5; Cat#04-1624
Mouse monoclonal anti-gamma tubulin	Sigma-Aldrich	Clone GTU-88; Cat#T6557
Mouse monoclonal anti-acetylated tubulin	Sigma-Aldrich	Clone 6-11B-1; Cat #T7451
Mouse polyclonal anti-Nesprin1	[23]	Nes1M5
Rabbit polyclonal anti-Nesprin1	[23]	Nes1HAA12
Rabbit polyclonal anti-Nesprin2	[49]	Nes2K2
Rabbit polyclonal anti-Sun1	[23]	Sun1RFA1
Rabbit polyclonal anti-Sun2	This paper	Sun2CCA13
Alexa594-conjugated donkey anti-Rabbit	Thermofisher	Cat#A21207
Alexa594-conjugated donkey anti-Goat	Thermofisher	Cat#A11058
Alexa594-conjugated donkey anti-mouse	Thermofisher	Cat#A21203
Alexa488-conjugated donkey anti-Rabbit	Thermofisher	Cat#A21206
Alexa488-conjugated donkey anti-Goat	Thermofisher	Cat#A11055
Alexa488-conjugated donkey anti-mouse	Thermofisher	Cat#A21202
Alexa680-conjugated donkey anti-mouse	Thermofisher	Cat#A10038
Rabbit Fab Alexa 594 Fluoronanogold particles	Nanoprobes	Cat#7304
Chemicals, Peptides, and Recombinant Proteins		
Ketamine	Putney	Cat#26637041101

REAGENT or RESOURCE	SOURCE	IDENTIFIER
Xylazine	Santa Cruz Biotechnology	Cat#sc-253838
Atropin sulfate	Bausch&Lomb	Cat#AB05007
Gonak	Akorn	Cat#17478006412
DMEM	Sigma-Aldrich	Cat#D5796
Fetal Bovine serum	Atlanta Biologicals, Inc	N/A
100XPenicillin/Streptomycin	Thermofisher	Cat#15140122
Paraformaldehyde	Electron Microscopy Sciences	Cat#15710
Phosphate Buffer Saline	Thermofisher	Cat#14200-075
Lipofectamine SiRNA Max	Thermofisher	Cat#13778-030
OCT compound	Tissue-Tek	Cat#4583
Donkey serum	Sigma-Aldrich	Cat#D9663
Triton X-100	Sigma-Aldrich	Cat#T8284
4′,6-Diamidine-2′-phenylindole dihydrochloride (DAPI)	Sigma-Aldrich	Cat#32670
Fluorescent mounting medium	DAKO	Cat#S3023
Optimem	Thermofisher	Cat#11058-021
Lipofectamine 2000	Thermofisher	Cat#11668-027
Glutaraldehyde	Electron Microscopy Sciences	Cat#16216
Araldite resin	Electron Microscopy Sciences	Cat#13940
Low melt agarose	Sigma-Aldrich	Cat#A9414
Protease inhibitors	Roche	Cat#11836153001
Super Signal West Pico	Thermofisher	Cat#1856135
Protein A/G beads	Pierce	Cat#20423
Trizol	Thermofisher	Cat#15596020
Zirconium oxide beads	Next Advance	Cat#18064014
Superscript II	Thermofisher	Cat#
Taq HI-FI polymerase	Thermofisher	Cat#11304-011
Pronase E	Sigma-Aldrich	Cat# P5147
F12K nutrient mixture	Thermofisher	Cat# 21127030
DNase I	Sigma-Aldrich	Cat# DN25
DMEM/F12	Thermofisher	Cat# 11330-032
L-Glutamine	Thermofisher	Cat# 25030-149
Sodium bicarbonate	Thermofisher	Cat# 25080-094
Insulin	Sigma-Aldrich	Cat# I-6634
Epidermal growth factor	BD Biosciences	Cat# 354001
Apo-Transferrin	Sigma-Aldrich	Cat# T1147
Cholera toxin	Sigma-Aldrich	Cat# C8052
Bovine pituitary extract	Hammond Cell Tech	Cat# 1077
Retinoid acid	Sigma-Aldrich	Cat# R-2625
Transwell-Clear permeable filter supports	Corning	Cat# 3470

REAGENT or RESOURCE	SOURCE	IDENTIFIER
Fungizone	Thermofisher	Cat# 15290-018
Experimental Models: Cell Lines		
NIH3t3	ATCC	ATCC#CRL-1658
Experimental Models: Organisms/Strains		
Mouse: Rho-Cre	[18]	JAX#015850
Mouse: Rho−/−	[45]	N/A
Mouse: Actin-Cre	[46]	JAX#003376
Mouse:Chx10-Cre	[29]	JAX#005105
Mouse: Nesprin1f/f	[19]	N/A
MOUSE: CAG-LacZ/EGFP-KASH2	[50]	N/A
Oligonucleotides		
Nesprin1 DsiRNAs, 27 mer duplexes, TrifectA RNAi kit	Integrated DNA Technologies	mm.Ri. Syne1.13
Nesprin1α 5′primer: 5′-TCCAGGAAGGACTGAGCCTT-3′	Integrated DNA Technologies	N/A
Nesprin1Long 5′ primer: 5′GAGAACAAAATCCAGCTTCAGGAAATGGGAGAACGGC-3′	Integrated DNA Technologies	N/A
Nesprin1 3′ primer: 5′-CTTGTGTGGGGATGTCTGCT-3′	Integrated DNA Technologies	N/A
Recombinant DNA		
Myc-Rootletin	[30]	Addgene plasmid#41167
Root C1-2	This paper	N/A
Root C1-3	This paper	N/A
Root C1-4	This paper	N/A
EGFP-Nes1α	This paper	N/A
EGFP-Nes1αΔKASH	This paper	N/A
EGFP-KASH2	[27]	N/A
EGFP-KASH2ext	[27]	N/A
Software and Algorithms		
NIS-Elements, Nikon	N/A	N/A
TopHat2 V.2.0.5	[54]	N/A
Bowtie V.0.12.8	[55]	N/A
Samtools V.0.1.18	[56]	N/A
Bedtools v.2.23.0	[58]	N/A
Integrative genomic viewer	[57]	N/A
Allen Mouse Brain Atlas	[31]	N/A
Origin 8.5	OriginLab	N/A

Supplementary Material

Refer to Web version on PubMed Central for supplementary material.

Acknowledgments

We thank Belinda McMahan and Mike Casey from our departmental Morphology and Imaging Core and Molecular Biology Module (Dr. Tom Ferguson), the Mouse Genetics Core at Washington University (Dr. Mia Wallace) for mice breeding and genotyping and Robyn Roth from the dedicated team of the Washington University Center for Cellular Imaging (WUCCI, Dr. James Fitzpatrick). The authors are grateful to Dr. Ju Chen (university of California, San Diego) for the kind gift of Nes1$^{Flox/Flox}$ mice. This work was funded by the National Eye Institute (#EY022632 to D.H., #EY019312 and #EY025696 to V.J.K.), the National Institute of Diabetes and Digestive and Kidney Diseases (#R01DK108005 to M.R.M), a National Eye Institute Center Core Grant (#P30EY002687), and an unrestricted grant to the Department of Ophthalmology and Visual Sciences at Washington University from *Research to Prevent Blindness*. P.R. is supported by the National Eye institute (R01 EY012543 and T32 EY013360).

References

1. Apel ED, Lewis RM, Grady RM, Sanes JR. Syne-1, a dystrophin- and Klarsicht-related protein associated with synaptic nuclei at the neuromuscular junction. J Biol Chem. 2000; 275:31986–31995. [PubMed: 10878022]
2. Grady RM, Starr DA, Ackerman GL, Sanes JR, Han M. Syne proteins anchor muscle nuclei at the neuromuscular junction. Proc Natl Acad Sci U S A. 2005; 102:4359–4364. [PubMed: 15749817]
3. Zhang Q, Skepper JN, Yang F, Davies JD, Hegyi L, Roberts RG, Weissberg PL, Ellis JA, Shanahan CM. Nesprins: a novel family of spectrin-repeat-containing proteins that localize to the nuclear membrane in multiple tissues. J Cell Sci. 2001; 114:4485–4498. [PubMed: 11792814]
4. Starr DA, Han M. Role of ANC-1 in tethering nuclei to the actin cytoskeleton. Science. 2002; 298:406–409. [PubMed: 12169658]
5. Sosa BA, Rothballer A, Kutay U, Schwartz TU. LINC complexes form by binding of three KASH peptides to domain interfaces of trimeric SUN proteins. Cell. 2012; 149:1035–1047. [PubMed: 22632968]
6. Zhou Z, Du X, Cai Z, Song X, Zhang H, Mizuno T, Suzuki E, Yee MR, Berezov A, Murali R, et al. Structure of Sad1-UNC84 homology (SUN) domain defines features of molecular bridge in nuclear envelope. J Biol Chem. 2012; 287:5317–5326. [PubMed: 22170055]
7. Malone CJ, Fixsen WD, Horvitz HR, Han M. UNC-84 localizes to the nuclear envelope and is required for nuclear migration and anchoring during C. elegans development. Development. 1999; 126:3171–3181. [PubMed: 10375507]
8. Hodzic DM, Yeater DB, Bengtsson L, Otto H, Stahl PD. Sun2 is a novel mammalian inner nuclear membrane protein. J Biol Chem. 2004; 279:25805–25812. [PubMed: 15082709]
9. Haque F, Lloyd DJ, Smallwood DT, Dent CL, Shanahan CM, Fry AM, Trembath RC, Shackleton S. SUN1 interacts with nuclear lamin A and cytoplasmic nesprins to provide a physical connection between the nuclear lamina and the cytoskeleton. Mol Cell Biol. 2006; 26:3738–3751. [PubMed: 16648470]
10. Razafsky D, Hodzic D. Bringing KASH under the SUN: the many faces of nucleo-cytoskeletal connections. J Cell Biol. 2009; 186:461–472. [PubMed: 19687252]
11. Chang W, Worman HJ, Gundersen GG. Accessorizing and anchoring the LINC complex for multifunctionality. J Cell Biol. 2015; 208:11–22. [PubMed: 25559183]
12. Bone CR, Starr DA. Nuclear migration events throughout development. J Cell Sci. 2016; 129:1951–1961. [PubMed: 27182060]
13. Gros-Louis F, Dupre N, Dion P, Fox MA, Laurent S, Verreault S, Sanes JR, Bouchard JP, Rouleau GA. Mutations in SYNE1 lead to a newly discovered form of autosomal recessive cerebellar ataxia. Nat Genet. 2007; 39:80–85. [PubMed: 17159980]
14. Synofzik M, Smets K, Mallaret M, Di Bella D, Gallenmuller C, Baets J, Schulze M, Magri S, Sarto E, Mustafa M, et al. SYNE1 ataxia is a common recessive ataxia with major non-cerebellar features: a large multi-centre study. Brain. 2016; 139:1378–1393. [PubMed: 27086870]
15. Mademan I, Harmuth F, Giordano I, Timmann D, Magri S, Deconinck T, Claassen J, Jokisch D, Genc G, Di Bella D, et al. Multisystemic SYNE1 ataxia: confirming the high frequency and extending the mutational and phenotypic spectrum. Brain. 2016; 139:e46. [PubMed: 27197992]

16. Razafsky D, Hodzic D. A variant of Nesprin1 giant devoid of KASH domain underlies the molecular etiology of autosomal recessive cerebellar ataxia type I. Neurobiol Dis. 2015; 78:57–67. [PubMed: 25843669]
17. Liu Q, Tan G, Levenkova N, Li T, Pugh EN Jr, Rux JJ, Speicher DW, Pierce EA. The proteome of the mouse photoreceptor sensory cilium complex. Mol Cell Proteomics. 2007; 6:1299–1317. [PubMed: 17494944]
18. Li S, Chen D, Sauve Y, McCandless J, Chen YJ, Chen CK. Rhodopsin-iCre transgenic mouse line for Cre-mediated rod-specific gene targeting. Genesis. 2005; 41:73–80. [PubMed: 15682388]
19. Zhang J, Felder A, Liu Y, Guo LT, Lange S, Dalton ND, Gu Y, Peterson KL, Mizisin AP, Shelton GD, et al. Nesprin 1 is critical for nuclear positioning and anchorage. Hum Mol Genet. 2009; 19:329–341. [PubMed: 19864491]
20. Rajgor D, Mellad JA, Autore F, Zhang Q, Shanahan CM. Multiple novel nesprin-1 and nesprin-2 variants act as versatile tissue-specific intracellular scaffolds. PLoS One. 2012; 7:e40098. [PubMed: 22768332]
21. Duong NT, Morris GE, Lam le T, Zhang Q, Sewry CA, Shanahan CM, Holt I. Nesprins: tissue-specific expression of epsilon and other short isoforms. PLoS One. 2014; 9:e94380. [PubMed: 24718612]
22. Simpson JG, Roberts RG. Patterns of evolutionary conservation in the nesprin genes highlight probable functionally important protein domains and isoforms. Biochem Soc Trans. 2008; 36:1359–1367. [PubMed: 19021556]
23. Razafsky DS, Ward CL, Kolb T, Hodzic D. Developmental regulation of linkers of the nucleoskeleton to the cytoskeleton during mouse postnatal retinogenesis. Nucleus. 2013; 4:399–409. [PubMed: 23974729]
24. Holt I, Duong NT, Zhang Q, Lam le T, Sewry CA, Mamchaoui K, Shanahan CM, Morris GE. Specific localization of nesprin-1-alpha2, the short isoform of nesprin-1 with a KASH domain, in developing, fetal and regenerating muscle, using a new monoclonal antibody. BMC Cell Biol. 2016; 17:26. [PubMed: 27350129]
25. Yang J, Liu X, Yue G, Adamian M, Bulgakov O, Li T. Rootletin, a novel coiled-coil protein, is a structural component of the ciliary rootlet. J Cell Biol. 2002; 159:431–440. [PubMed: 12427867]
26. Razafsky D, Hodzic D. Temporal and tissue-specific disruption of LINC complexes in vivo. Genesis. 2014; 52:359–365. [PubMed: 24550182]
27. Stewart-Hutchinson PJ, Hale CM, Wirtz D, Hodzic D. Structural requirements for the assembly of LINC complexes and their function in cellular mechanical stiffness. Exp Cell Res. 2008; 314:1892–1905. [PubMed: 18396275]
28. Crisp M, Liu Q, Roux K, Rattner JB, Shanahan C, Burke B, Stahl PD, Hodzic D. Coupling of the nucleus and cytoplasm: role of the LINC complex. J Cell Biol. 2006; 172:41–53. [PubMed: 16380439]
29. Rowan S, Cepko CL. Genetic analysis of the homeodomain transcription factor Chx10 in the retina using a novel multifunctional BAC transgenic mouse reporter. Dev Biol. 2004; 271:388–402. [PubMed: 15223342]
30. Bahe S, Stierhof YD, Wilkinson CJ, Leiss F, Nigg EA. Rootletin forms centriole-associated filaments and functions in centrosome cohesion. J Cell Biol. 2005; 171:27–33. [PubMed: 16203858]
31. Lein ES, Hawrylycz MJ, Ao N, Ayres M, Bensinger A, Bernard A, Boe AF, Boguski MS, Brockway KS, Byrnes EJ, et al. Genome-wide atlas of gene expression in the adult mouse brain. Nature. 2007; 445:168–176. [PubMed: 17151600]
32. Mahjoub MR, Xie Z, Stearns T. Cep120 is asymmetrically localized to the daughter centriole and is essential for centriole assembly. J Cell Biol. 2010; 191:331–346. [PubMed: 20956381]
33. Mohan S, Timbers TA, Kennedy J, Blacque OE, Leroux MR. Striated rootlet and nonfilamentous forms of rootletin maintain ciliary function. Curr Biol. 2013; 23:2016–2022. [PubMed: 24094853]
34. Chen JV, Kao LR, Jana SC, Sivan-Loukianova E, Mendonca S, Cabrera OA, Singh P, Cabernard C, Eberl DF, Bettencourt-Dias M, et al. Rootletin organizes the ciliary rootlet to achieve neuron sensory function in Drosophila. J Cell Biol. 2015; 211:435–453. [PubMed: 26483560]

35. Yang J, Gao J, Adamian M, Wen XH, Pawlyk B, Zhang L, Sanderson MJ, Zuo J, Makino CL, Li T. The ciliary rootlet maintains long-term stability of sensory cilia. Mol Cell Biol. 2005; 25:4129–4137. [PubMed: 15870283]
36. Noreau A, Bourassa CV, Szuto A, Levert A, Dobrzeniecka S, Gauthier J, Forlani S, Durr A, Anheim M, Stevanin G, et al. SYNE1 mutations in autosomal recessive cerebellar ataxia. JAMA neurology. 2013; 70:1296–1231. [PubMed: 23959263]
37. Izumi Y, Miyamoto R, Morino H, Yoshizawa A, Nishinaka K, Udaka F, Kameyama M, Maruyama H, Kawakami H. Cerebellar ataxia with SYNE1 mutation accompanying motor neuron disease. Neurology. 2013; 80:600–601. [PubMed: 23325900]
38. Wiethoff S, Hersheson J, Bettencourt C, Wood NW, Houlden H. Heterogeneity in clinical features and disease severity in ataxia-associated SYNE1 mutations. J Neurol. 2016; 263:1503–1510. [PubMed: 27178001]
39. Ozoguz A, Uyan O, Birdal G, Iskender C, Kartal E, Lahut S, Omur O, Agim ZS, Eken AG, Sen NE, et al. The distinct genetic pattern of ALS in Turkey and novel mutations. Neurobiology of aging. 2015; 36:1764 e1769–1718.
40. Attali R, Warwar N, Israel A, Gurt I, McNally E, Puckelwartz M, Glick B, Nevo Y, Ben-Neriah Z, Melki J. Mutation of SYNE-1, encoding an essential component of the nuclear lamina, is responsible for autosomal recessive arthrogryposis. Hum Mol Genet. 2009 in press.
41. Waters AM, Beales PL. Ciliopathies: an expanding disease spectrum. Pediatric nephrology. 2011; 26:1039–1056. [PubMed: 21210154]
42. Luxton GW, Gomes ER, Folker ES, Vintinner E, Gundersen GG. Linear arrays of nuclear envelope proteins harness retrograde actin flow for nuclear movement. Science. 2010; 329:956–959. [PubMed: 20724637]
43. Luxton GW, Gomes ER, Folker ES, Worman HJ, Gundersen GG. TAN lines: a novel nuclear envelope structure involved in nuclear positioning. Nucleus. 2011; 2:173–181. [PubMed: 21818410]
44. Espigat-Georger A, Dyachuk V, Chemin C, Emorine L, Merdes A. Nuclear alignment in myotubes requires centrosome proteins recruited by nesprin-1. J Cell Sci. 2016
45. Lem J, Krasnoperova NV, Calvert PD, Kosaras B, Cameron DA, Nicolo M, Makino CL, Sidman RL. Morphological, physiological, and biochemical changes in rhodopsin knockout mice. Proc Natl Acad Sci U S A. 1999; 96:736–741. [PubMed: 9892703]
46. Lewandoski M, Meyers EN, Martin GR. Analysis of Fgf8 gene function in vertebrate development. Cold Spring Harb Symp Quant Biol. 1997; 62:159–168. [PubMed: 9598348]
47. Razafsky D, Potter C, Hodzic D. Validation of a Mouse Model to Disrupt LINC Complexes in a Cell-specific Manner. J Vis Exp. 2015
48. Razafsky D, Blecher N, Markov A, Stewart-Hutchinson PJ, Hodzic D. LINC complexes mediate the positioning of cone photoreceptor nuclei in mouse retina. PLoS One. 2012; 7:e47180. [PubMed: 23071752]
49. Khatau SB, Bloom RJ, Bajpai S, Razafsky D, Zang S, Giri A, Wu PH, Marchand J, Celedon A, Hale CM, et al. The distinct roles of the nucleus and nucleus-cytoskeleton connections in three-dimensional cell migration. Sci Rep. 2012; 2:488. [PubMed: 22761994]
50. Razafsky D, Potter C, Hodzic D. Validation of a Mouse Model to Disrupt LINC Complexes in a Cell-specific Manner. J Vis Exp. 2015:e53318. [PubMed: 26710083]
51. Silva E, Betleja E, John E, Spear P, Moresco JJ, Zhang S, Yates JR 3rd, Mitchell BJ, Mahjoub MR. Ccdc11 is a novel centriolar satellite protein essential for ciliogenesis and establishment of left-right asymmetry. Mol Biol Cell. 2016; 27:48–63. [PubMed: 26538025]
52. Roger JE, Hiriyanna A, Gotoh N, Hao H, Cheng DF, Ratnapriya R, Kautzmann MA, Chang B, Swaroop A. OTX2 loss causes rod differentiation defect in CRX-associated congenital blindness. J Clin Invest. 2014; 124:631–643. [PubMed: 24382353]
53. Ruzycki PA, Tran NM, Kefalov VJ, Kolesnikov AV, Chen S. Graded gene expression changes determine phenotype severity in mouse models of CRX-associated retinopathies. Genome Biol. 2015; 16:171. [PubMed: 26324254]

54. Kim D, Pertea G, Trapnell C, Pimentel H, Kelley R, Salzberg SL. TopHat2: accurate alignment of transcriptomes in the presence of insertions, deletions and gene fusions. Genome Biol. 2013; 14:R36. [PubMed: 23618408]

55. Langmead B, Trapnell C, Pop M, Salzberg SL. Ultrafast and memory-efficient alignment of short DNA sequences to the human genome. Genome Biol. 2009; 10:R25. [PubMed: 19261174]

56. Li H, Handsaker B, Wysoker A, Fennell T, Ruan J, Homer N, Marth G, Abecasis G, Durbin R, Genome Project Data Processing, S. The Sequence Alignment/Map format and SAMtools. Bioinformatics. 2009; 25:2078–2079. [PubMed: 19505943]

57. Robinson JT, Thorvaldsdottir H, Winckler W, Guttman M, Lander ES, Getz G, Mesirov JP. Integrative genomics viewer. Nat Biotechnol. 2011; 29:24–26. [PubMed: 21221095]

58. Quinlan AR, Hall IM. BEDTools: a flexible suite of utilities for comparing genomic features. Bioinformatics. 2010; 26:841–842. [PubMed: 20110278]

59. Vierstra J, Rynes E, Sandstrom R, Zhang M, Canfield T, Hansen RS, Stehling-Sun S, Sabo PJ, Byron R, Humbert R, et al. Mouse regulatory DNA landscapes reveal global principles of cis-regulatory evolution. Science. 2014; 346:1007–1012. [PubMed: 25411453]

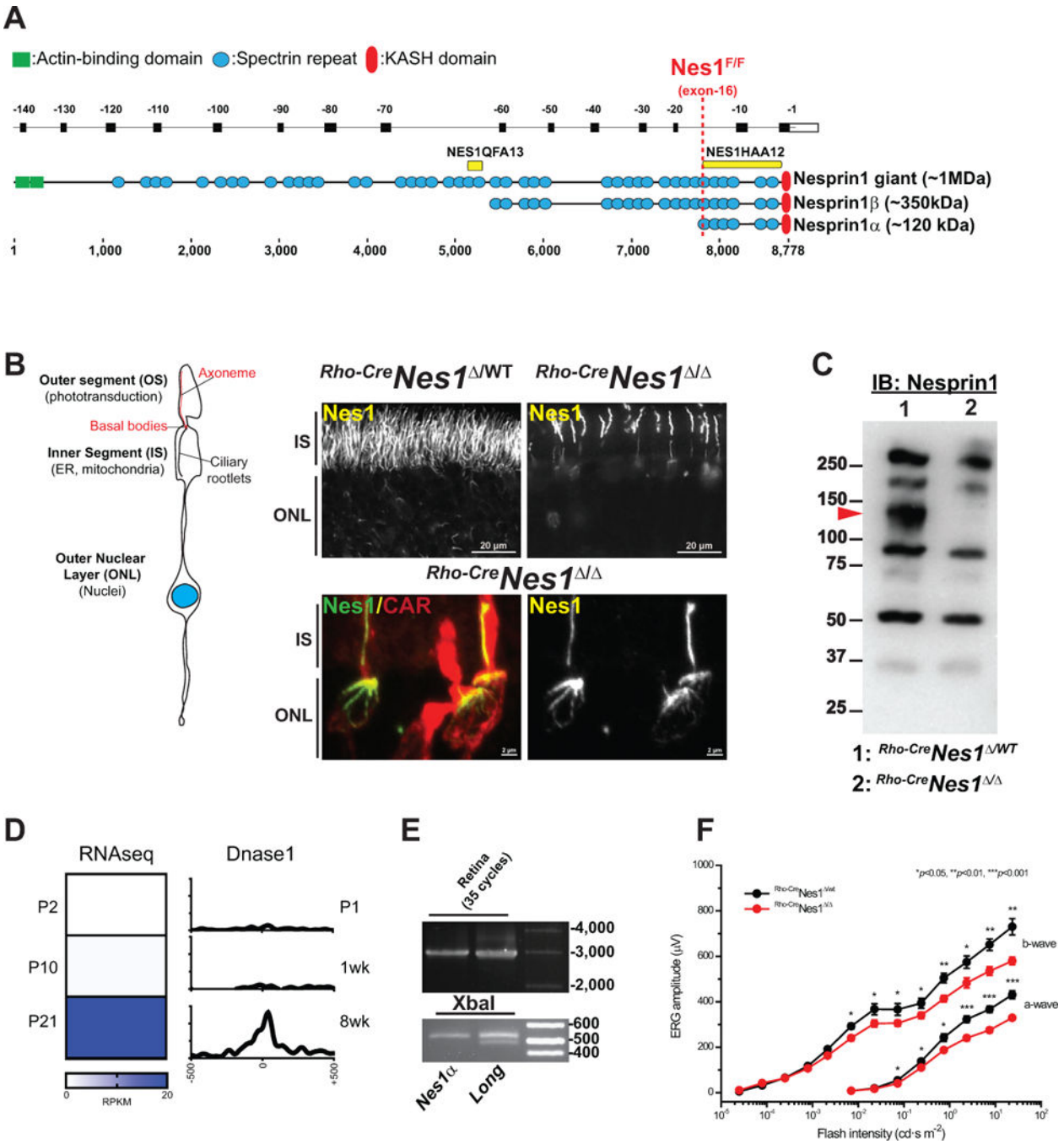

Figure 1. Nesprin1α forms filamentous structures in photoreceptors

A. Alignment of *Syne1* exons (top, reverse numbering) with corresponding Nesprin1 isoforms that interact with the NE through their C-terminal KASH domain. Yellow bars: epitopes used to raise NES1QFA13 and Nes1HAA12 antisera. The dashed red line denotes the position of LoxP sites flanking exon -16 in Nes1$^{Flox/Flox}$ mice. **B.** Depiction of the main compartments of photoreceptors. Nesprin1 immunolabeling of adult $^{Rho\text{-}Cre}Nes1^{\Delta/WT}$ (top left panel) and $^{Rho\text{-}Cre}Nes1^{\Delta/\Delta}$ (top right panel) littermate retinas. Note the loss of Nesprin1 immunoreactivity in the IS and the ONL of $^{Rho\text{-}Cre}Nes1^{\Delta/\Delta}$ rods. Lower panels: Maximum

intensity projection of Nesprin1 localization in cones within *Rho-Cre*$Nes1^{\Delta/\Delta}$ retinas emphasizing similar Nesprin1 filaments lining the IS and “aster-like” structures capping the apical side of cone nuclei. CAR: Cone arrestin used to label cones. IS: inner segments; ONL: outer nuclear layer. See also Figure S1A and S1B. **C.** Nesprin1 immunobloting of adult *Rho-Cre*$Nes1^{\Delta/WT}$ and *Rho-Cre*$Nes1^{\Delta/\Delta}$ retina lysates showing the loss of a ~120 kDa immunoreactive band in *Rho-Cre*$Nes1^{\Delta/\Delta}$ retinas (arrowhead). See also Figure S1C and S1D. **D.** Left: Relative abundance (in reads per kilobase per million mapped reads, RPKM) of reads encompassing exon-16b, which is specifically included in Nesprin1α transcripts, at different postnatal (P) stages of retinal development. Right: DNase I hypersensitivity (reads per base per million) at similar developmental stages showing the corresponding activation of the Nesprin1α promoter. **E:** Upper panel: RT-PCR amplification (35 cycles) of Nesprin1α (Nes1α) or of transcripts encoding larger isoforms of Nesprin1 (Long) performed on total RNA from retina (see also Figure S1E, F for more details). Lower panel: XbaI digests emphasizing the absence of the 476 bp restriction fragments (asterisk) indicative of exon-2 alternative splicing in retinal Nesprin1α transcripts. See also Figure S1E and S1F. **F.** Scotopic electroretinograms of 2.5 month-old *Rho-Cre*$Nes1^{\Delta/\Delta}$ (red traces; n=4) and *Rho-Cre*$Nes1^{\Delta/WT}$ (black traces; n=4) mice. Note a ~20% decrease of ERG a- and b-waves amplitudes in *Rho-Cre*$Nes1^{\Delta/\Delta}$ mice compared to controls.

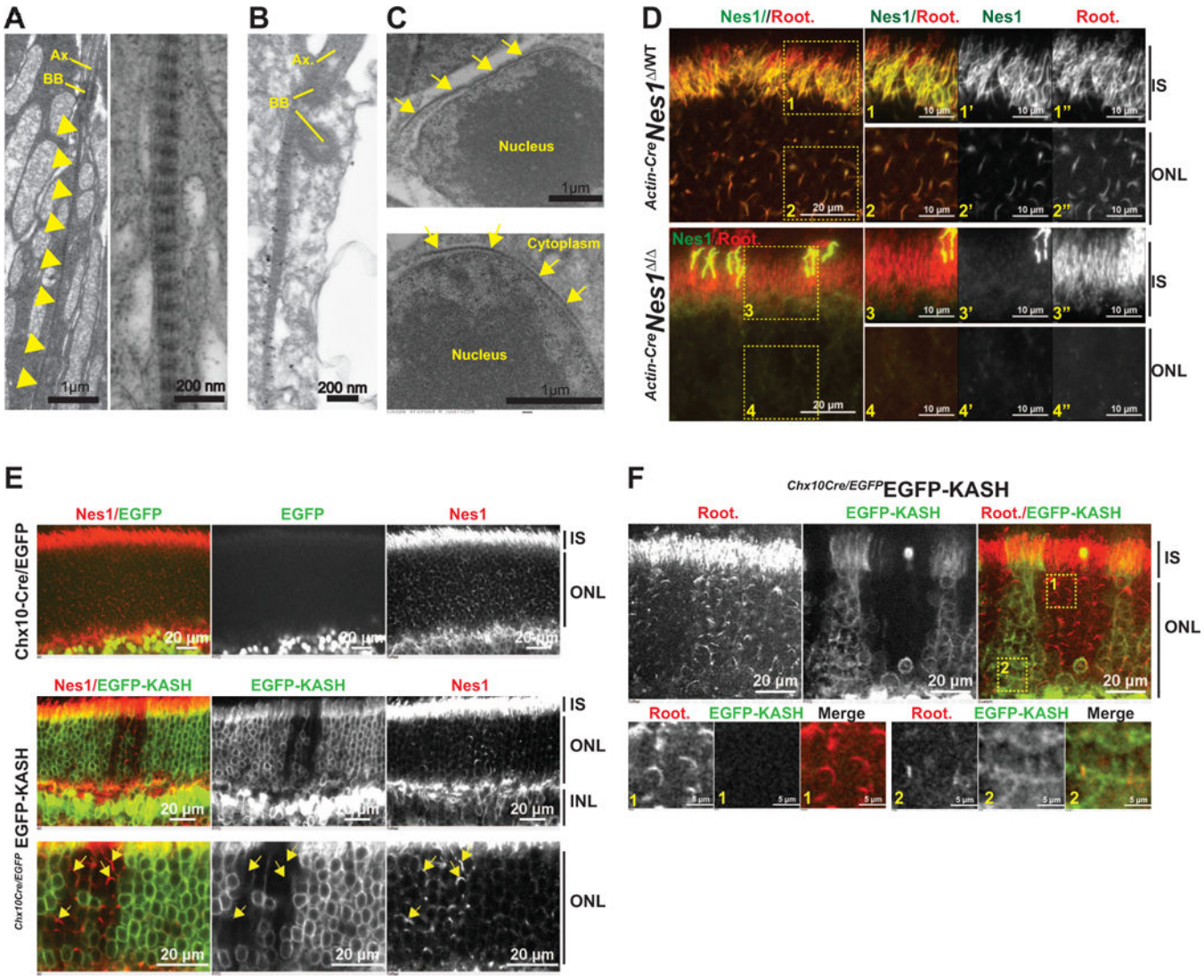

Figure 2. Nesprin1α colocalizes with photoreceptors ciliary rootlets and recruits perinuclear filaments of rootletin

A. Transmission electron microscopy (TEM) of IS from wild-type C57/Bl6 retinas. Left panel: striated filaments of rootletin (arrowheads) forming the ciliary rootlets that line the IS of wild-type rod photoreceptors. Right panel: Zoomed in view of the striated rootletin network showing long fibrils cross-linked by regularly spaced electron-dense striations. BB: basal bodies, Ax.: axoneme. **B.** Nesprin1 immunogold labeling of a rod IS showing the colocalization of gold particles with ciliary rootlets of photoreceptors. **C.** TEM of perinuclear striated filaments of rootletin lining the nuclear surface of rods (arrows). **D.** Nesprin1 and rootletin immunolabeling of $^{Actin\text{-}Cre}Nes1^{\Delta/WT}$ (top panels) and $^{Actin\text{-}Cre}Nes1^{\Delta/\Delta}$ retinas (bottom panels). Arrow in inset 3 point to a cross-reaction of Nesprin1 antibodies with cone OS. **E.** Top: Nesprin1 immunofluorescence of Chx10-Cre/EGFP retinas. Note the GFP fluorescence originating from the permanent expression of GFP-tagged Cre recombinase in bipolar cells. Bottom panels: Nesprin1 immunofluorescence of $^{Ch10x\text{-}Cre}$EGFP-KASH retinas showing that Nesprin1 filaments are exclusively detected at

the nuclear periphery of rods that do not express EGFP-KASH (arrows, bottom panel). INL: inner nuclear layer. **F.** *Ch10x-Cre*EGFP-KASH retinas immunolabeled with rootletin showing the exclusive retention of rootletin filaments at the nuclear periphery of rods that do not express EGFP-KASH. Lower panels: zoomed views of rootletin immunofluorescence in ONL regions devoid of (1) or expressing (2) EGFP-KASH.

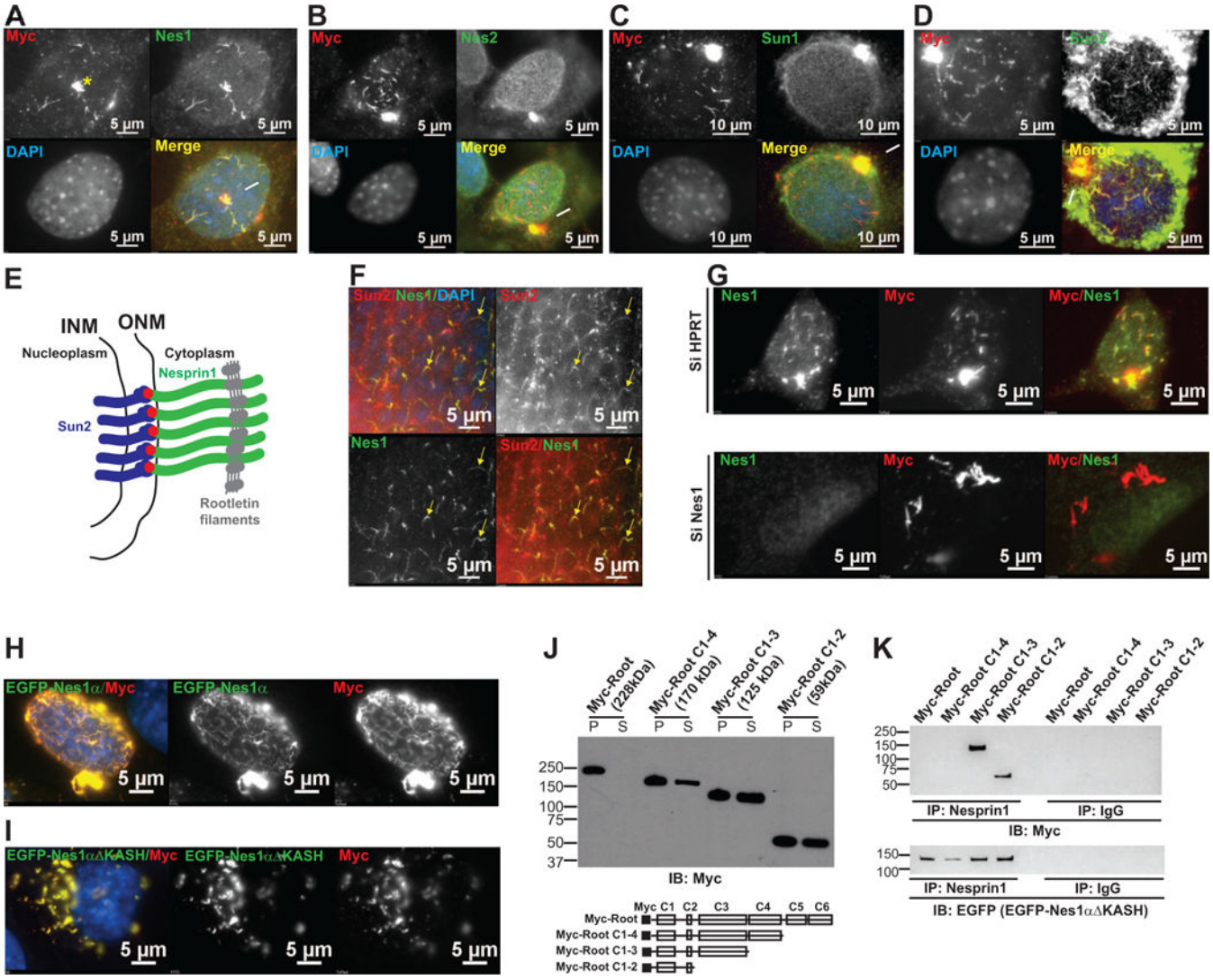

Figure 3. Recombinant rootletin filaments recruit multiple isoforms of Nesprin1

A. Nesprin1 and Myc colabelling of NIH3t3 cells transfected with Myc-root. Note the NE aggregation and centrosome recruitment of Nesprin1 by Myc-root filaments. See also Figure S2A,B. **B, C, D**. Same colabelling experiment with antibodies against Nesprin2 (B), Sun1 (C) or Sun2 (D) at the NE. Note that whereas the NE localization of Nesprin2 and Sun1 is not affected by Myc-root filaments, Sun2 aggregates into NE Myc-root/Nesprin1 filaments. See also Figures S2D–G. **E.** Model of Sun2/Nesprin1 LINC complexes that dock perinuclear rootletin filaments at the nuclear surface of rods and of NIH3t3 cells transfected with Myc-root. Red dots: KASH domains. **F.** Nesprin1 and Sun2 colabelling of the ONL of C57/Bl6 retinas. Note the discrete colocalization of Sun2 with Nesprin1 filaments (arrows). **G.** Myc and Nesprin1 coimmunolabeling of NIH3t3 cells transfected either with control SiHPRT (top) or with SiNes1 (bottom) SiRNAs for 36h and subsequently with Myc-root for 12h. Note the lack of rootletin filaments at the nuclear surface in the absence of Nesprin1 expression and their accumulation in the cytoplasm. See also Figure S2H. **H, I:** Basal views of NIH3t3 cotransfected with Myc-root and either EGFP-Nes1α (H) or EGFP-

Nes1αΔKASH (I). Note that whereas EGFP-Nes1α and rootletin filaments essentially colocalize at the NE, EGFP-Nes1αΔKASH colocalizes with rootletin filaments in the cytoplasm. **J:** Volume to volume partition into pellets (P) and supernatant (S) of Myc-Root deletion mutants extracted with RIPA buffer from transfected NIH3t3 cells. Bottom: depiction of the coiled-coil domains of Myc-root (C1 to C6) and of each deletion mutant. **K**: Nesprin1 and rabbit immunoglobulins (IgG, used as a negative control) immunoprecipitations (IP) of RIPA lysates from NIH3t3 cells cotransfected with EGFP-Nes1αΔKASH and indicated Myc-Root deletion constructs. Immunoprecipitates were immunoblotted (IB) either with Myc (top panel) or with EGFP (bottom panel) antibodies to detect deletion mutants of Myc-Root and EGFP-Nes1αΔKASH, respectively. See also Figure S2I.

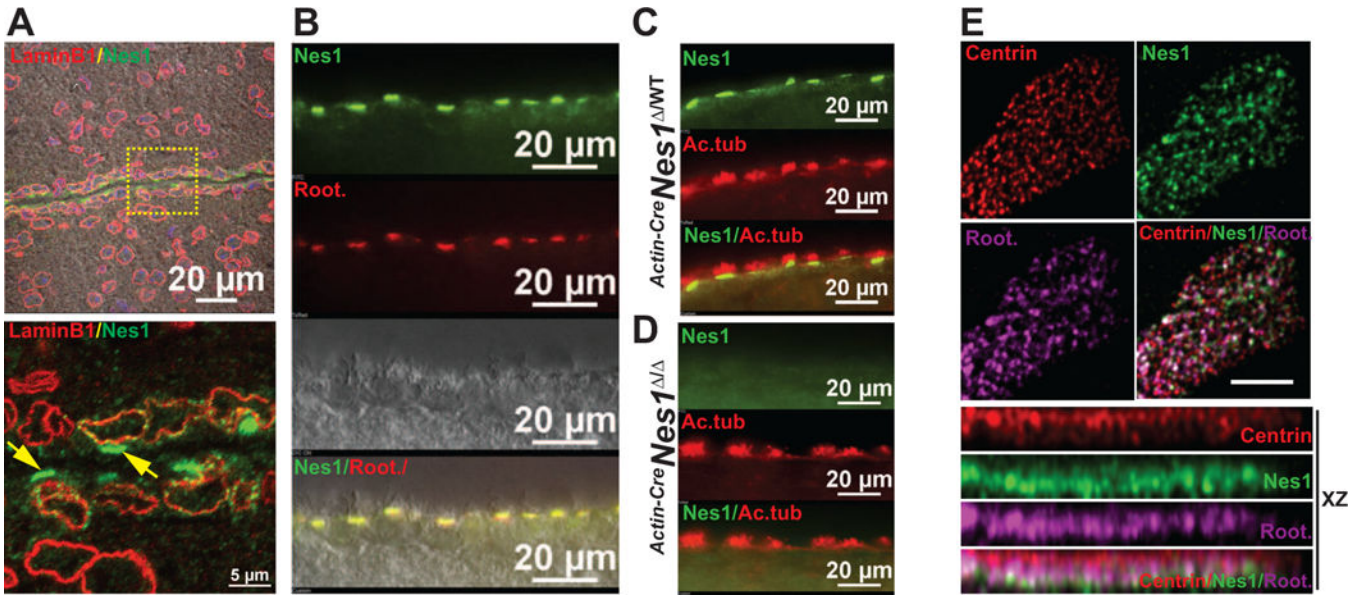

Figure 4. Nesprin1 is a widespread component of ciliary rootlets

A. Nesprin1 and Lamin B1 immunolabeling of ependymal cells lining the lumen of wild-type brain ventricles. Note the bright staining of Nesprin1 arrays on the apical side of ependymal cells lining the ventricular lumen (arrows in inset). **B**. Colocalization of Nesprin1 with ciliary rootlets of ependymal cells labeled with rootletin **C.** Localization of Nesprin1 underneath ciliary axonemes of ependymal cells cilia labeled with acetylated tubulin (Ac.tub). **D**. Same experiments as in (C) performed on $^{Actin\text{-}Cre}Nes1^{\Delta/\Delta}$ brains. Note the absence of Nesprin1 immunoreactivity at ciliary rootlets. **E.** Apical view of a single multiciliated MTEC colabeled with Centrin, Nesprin1 and Rootletin (top). Note the colocalization of rootletin and Nesprin1 just underneath the array of basal bodies labeled with Centrin in XZ projections (bottom).